Symmetry Reduction and Shape Effects in Concave Chiral Plasmonic Structures

Gary W. Paterson,[*,†] Affar S. Karimullah,[‡] Scott G. Smith,[†] Malcolm Kadodwala,[‡] and Donald A. MacLaren[*,†]

SUPA, School of Physics and Astronomy, University of Glasgow, Glasgow G12 8QQ, UK., and School of Chemistry, University of Glasgow, Glasgow G12 8QQ, UK.

E-mail: gary.paterson@glasgow.ac.uk; dmaclaren@physics.org

[*]To whom correspondence should be addressed
[†]SUPA, School of Physics and Astronomy, University of Glasgow, Glasgow G12 8QQ, UK.
[‡]School of Chemistry, University of Glasgow, Glasgow G12 8QQ, UK.

Abstract

Chiral metamaterials have shown a number of interesting properties which result from the interaction of the chiral near-field they produce with light and mater. We investigate the influence of structural imperfections on the plasmonic properties of a chiral gold 'gammadion', using electron energy loss spectroscopy to directly inform simulations of realistic, imperfect structures. Unlike structures of simple convex geometry, the lowest energy modes of the ideal concave gammadion have a quadrupole and dipole character, with the mode energies determined by the nature of electrostatic coupling between the gammadion arms. These modes are strongly affected by structural imperfections that are inherent to the material properties and lithographic patterning. Even subwavelength-scale imperfections reduce the symmetry, lift mode degeneracies, convert dark modes into bright ones, and significantly alter the mode energy, its near-field strength and chirality. Such effects will be common to a number of multi-tipped concave structures currently being investigated for the chiral fields they support.

Keywords

metamaterial, plasmon, chiral, gammadion, symmetry, electron energy loss spectroscopy, scanning transmission electron microscopy, aloof excitation, concave

Introduction

Nanostructured plasmonic metamaterials have a diversity of potential applications, including optoelectronics, communications, sensing and biomedicine.[1,2] Lithographically patterned metals allow complex nanostructures to be formed - and correspondingly complex plasmonic resonances to be supported - but the resulting structures can deviate from their design due to limitations of the fabrication process and material properties such as grain size.[3] These, in turn, affect the nature of the plasmonic performance, even though the dimensions of imperfections may be only a few nanometres, far below optical wavelengths. Indeed, although

simulations often consider idealised, 'perfect' structures, deliberate changes in shape have been shown to cause mode energy shifts and splitting,[4–6] and fabrication defects can underpin the appearance of chiral modes in an achiral design.[7]

Various designs have been evaluated through simulation for use as chiral plasmonic nanostructures.[8] The gammadion, a symmetric, four-armed structure, with each arm shaped like the Greek letter Γ, has been investigated theoretically[9] and has potential use in optical nanofocusing and polarising components,[10] and as a probe of chiral supramolecular structure in biomolecules.[11–13] The latter is achieved through the enhanced superchiral electromagnetic fields[14,15] generated around the molecules by optical excitation of localised surface plasmon resonance (LSPR) modes; and understanding these fields in realistic structures is one motivation for the present work.

In this work, we use electron energy loss spectroscopy (EELS) in scanning transmission electron microscopy (STEM) to characterise the plasmonic excitations of real gammadia[11] fabricated on a thin Si_3N_4 substrate. Unlike optical techniques, EELS provides a means of mapping directly both bright and dark modes[16] (that is, modes with no net dipole moment) with high spatial resolution and has thus proven to be a powerful tool in plasmonics research.[17,18] Symmetry analysis and numerical calculations are used to relate the experimentally observed modes to those predicted for the ideal gammadion. The excellent spatial resolution of STEM measurements allows the three-dimensional shape of the structure to be determined[19] and for the measured nanofabrication defects to be incorporated into more realistic simulations. Despite modest, only nanoscale structural imperfections, we find substantial variations in the properties and chirality of the plasmonic modes.

Methods

Structure and Fabrication. The structure used in this work was fabricated in the James Watt Nanofabrication Facility at Glasgow on an approximately 38 nm thick silicon nitride

(Si_3N_4) TEM window using standard planar electron beam lithography techniques and comprised 60 nm of Au on a 2 nm Ti adhesion layer. The pattern was written in a bi-layer of PMMA resist using a Vistec VB6 UHR EWF with a spot size of < 4 nm. The metals were deposited by electron beam evaporation and the pattern formed by standard lift-off protocols.

TEM Measurements. Electron energy loss spectroscopy (EELS) measurements were performed in a probe corrected JEOL ARM 200F scanning transmission electron microscope operated at 200 keV and equipped with a cold field emission electron gun. The EELS spectra were collected using a GIF Gatan Quantum ER spectrometer in scanning TEM (STEM) mode, with a spatial resolution of 2.5 nm, a dispersion of 0.025 eV, and a pixel time of 0.1 s. The objective lens was off during the measurements and the convergence and collection semi-angles were 1.3 and 31 mrad, respectively. The electron extraction voltage was reduced to minimise the energy spread due to coulombic interactions in the electron beam,[20,21] to give a full width half maximum energy spread in the beam of 0.43 eV. Data were collected using the spectrum imaging methodology, with a pause between collection of successive rows of the dataset to minimise after-glow effects in the spectrometer: see our previous description for details.[19] The energy resolution of the EELS data was improved by iteratively performing Richardson-Lucy deconvolution[22] using averaged spectra from a bare section of the Si_3N_4 membrane as the kernel, after applying a Hann window taper to the data. This reduced the energy spread due to the finite energy distribution of the source electrons and broadening in the imaging system by a factor of 2.5 to 0.17 eV after deconvolution. By masking the experimental data and using aloof excitations, artefacts arising from the deconvolution process were also reduced. To make comparisons between experiment and simulations fair, simulated loss data are artificially broadened by cross-correlating the data with the Si_3N_4 kernel after self-deconvolution.

Simulations and Analysis. Simulations of EELS probabilities, optical scattering cross-sections, and electric field distributions from different nanostructures were performed using

the MNPBEM toolbox[23] with EELS classes[24] for MATLAB. The toolbox uses the boundary element method[17,25] to efficiently solve Maxwell's equations on meshed structures in isotropic and homogeneous dielectric environments. With the exception of the eigenmode simulations, all simulations used the 'bemret' solver, which solves the full Maxwell equations, and so includes retardation effects resulting from differences in plasmon phase across the sample.

Tabulated values[26] supplied with the program were used for the dielectric function of gold. A Si_3N_4 substrate with a dielectric constant of 4 was included in all BEM simulations, but no Ti adhesion layer was included. Absorption of the plasmon near-field by adhesion layers damps and broadens the resonance, reduces the field amplitude, and decreases the mode energy.[27] This may result in small energy offsets between the experimental and simulated data, but comparisons between the simulated results should be unaffected.

The 'ideal' and 'rounded' structures were meshed directly within the toolbox. For the experimentally observed 'real' structure, we used a similar procedure to that as described in our earlier work[19] but with meshing performed in OpenFlipper.[28] EELS data were used to determine the 't/λ' values (i.e. thickness over electronic mean free path length) across the 'real' structure, using interpolation at noisy points and scaled to the thickness measured independently by atomic force microscopy. All experimental and simulated spectra were processed using the Python programming language and the open source multidimensional data analysis toolbox HyperSpy.[29]

Ideal Gammadia

We begin by describing the plasmonic modes using a group theory analysis.[30,31] The ideal isolated gammadion has C_{4h} point group symmetry and so is not chiral, but provides a useful comparison to categorise distinct plasmonic modes. In practice, the presence of a substrate reduces the symmetry to the chiral C_4 subgroup, and structural imperfections further reduce symmetry to C_1, but the plasmonic modes supported still typically retain some C_{4h} character.

Figure 1 summarises a group-theoretical analysis of the possible low-energy plasmonic excitations in a planar gammadion. Here, we concentrate on in-plane charge displacements, since out-of-plane charge displacements in these relatively thin structures will produce higher energy modes that do not couple strongly to light. The left-hand column shows the symmetry adapted linear combination (SALC) of a basis of a single charge on a gammadion arm, which produces four modes: a monopole, a quadrupole and a doubly-degenerate dipole. The A^1 monopole mode is forbidden due to it having a net charge, but it shares the same symmetry as breathing modes, which have a compensating negative charge in the centre of the structure. Breathing modes have been observed previously in discs,[32] while pseudo-breathing or cavity modes are supported in other, non-circular 2-D structures.[33,34] Indeed, the higher-energy A^2 mode (top-right of Fig. 1) spans the same irreducible representation and could also be termed a 'breathing' mode. Other higher energy modes can be formed by considering the symmetry-allowed combinations of a dipole in each arm, producing a further four (2 singly- and 1 doubly-degenerate) modes spanning the same representations, as illustrated in the right-hand column. An important characteristic of the modes in the right-hand column is the nature of electrostatic coupling between the gammadion arms. As we will show, this *intra*-structural coupling across the gaps between the tips and elbows of adjacent arms is similar to *inter*-structural coupling observed between adjacent separate particles, where the relative orientation of the dipoles in each particle leads to the formation of a lower energy 'bonding' mode and a higher energy 'antibonding' mode, in analogy with molecular orbital theory.[35] Accordingly, we refer to the modes in the right hand column of Figure 1 as a 'bonding' mode (A^2), an 'antibonding' mode (B^2), and a 'mixed' mode (E^2), the last of which has both 'bonding' and 'antibonding' interactions between successive arms.

Symmetry analysis can reveal the shape of allowed modes but tells us nothing of their energetics. Generally, for a given structural length, modes with a greater number of nodal lines in the charge distribution will be of higher energy. In addition, *intra*-structural coupling can be expected to have significant influence in these concave structures. Concave structures

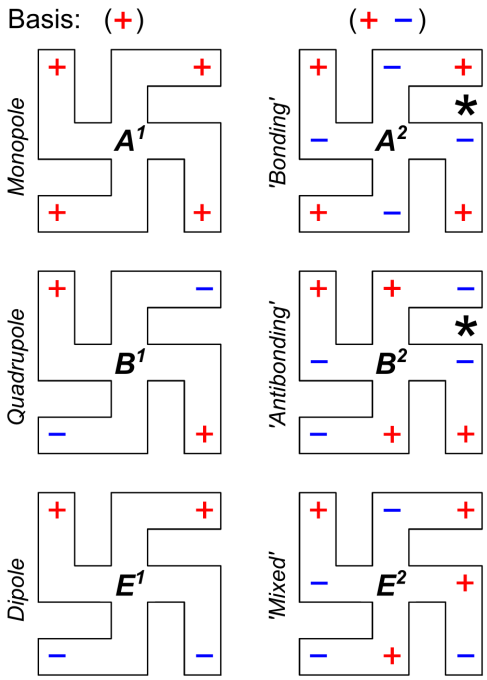

Figure 1: Low-energy planar excitations supported by the gammadion structure, labelled with C_4 point group irreducible representations (superscripts allow numbering of modes sharing the same symmetry). A basis of (left column) a single charge and (right column) a dipole along each gammadion arm yields A, B, and doubly-degenerate E modes. Typically, the two E^1 or E^2 modes are excited simultaneously, so the reducible real representation is illustrated in each column. Note that at the position of the asterisk, the coupling between arms differs: in the 'bonding' mode, a positive charge on one arm is aligned with a negative charge on the next; in the 'antibonding' mode, charges of the same sign are aligned.

differ from convex ones in that the former have at least one internal angle greater than 180°, forming an inwardly-curving surface or 'notch' that allows field coupling between different parts of the single structure, such as across the gap between gammadion arms indicated by the asterisks in Fig. 1. Examples of convex and other concave structures are depicted in Figure S1, where the largest internal angle of each structure within a category increases from left to right. While the character of the modes of a given structure will depend on its symmetry, the intra-structural coupling strength will depend on the precise geometry and, as we will show, this coupling can be modified to tailor the mode energies.

To understand the surface charge distributions and energetics of the LSPR modes of the gammadion, we performed an eigenmode analysis of the ideal C_{4h} structure designed for the

experiment. The results are summarised in Figure 2, which shows the gammadion dimensions in the bottom left panel. The eigenmodes for the isolated structure are presented in the top row of Figure 2, and are ordered by eigenvalue, λ, which increases with energy from left to right. An important, and perhaps surprising result is that the lowest energy eigenmode has quadrupolar symmetry, which is stabilised by electrostatic coupling between adjacent arms. The quadrupole has alternating positive and negative charges in successive arms so that each arm can couple to opposing charges on either side; in comparison, the dipole excitation will typically have two positive neighbouring arms and two negative neighbouring arms since the two degenerate irreducible E^1 modes are generally excited simultaneously. Such stabilization of the quadrupole mode does not occur in simpler structures with convex geometry, such as the square[33] or disc,[32] where coupling of this sort is naturally absent and the lowest energy mode is dipolar. To demonstrate this, in Figure 3 a gammadion is morphed into a square by filling in the void between adjacent arms, as shown in the abscissa. As the square geometry is approached, all mode energies increase because the electronic path length between all corners is reduced, even though the direct corner-to-corner distance is unchanged. Intra-structural coupling also reduces as the gap is filled, so that the first two modes reverse order, leaving the dipole mode as the square's lowest energy mode, as expected.

Also noted in Figure 2 are the dipole moments, $\mathrm{P_e}$, of each gammadion mode. Only the E modes support a net dipole moment and thus couple to light; all others have zero moment and are entirely dark in the perfect structure. The E^1 (dipole-like) mode has the largest moment and one might expect it to dominate an optical spectrum. The 'mixed' E^2 mode is also optically bright but has a lower moment because of the reduction of charge separation.

The lower panels of Figure 2 show the influence of a substrate on the above modes of the ideal gammadion. The choice of substrate varies depending on the application, but is generally a dielectric in which the plasmon propagation length is low; here we use a 38 nm thick SiN membrane to match experiments. The eigenmodes retain similar in-plane charge distributions to those supported by the isolated gammadion. However, an induced out-of-

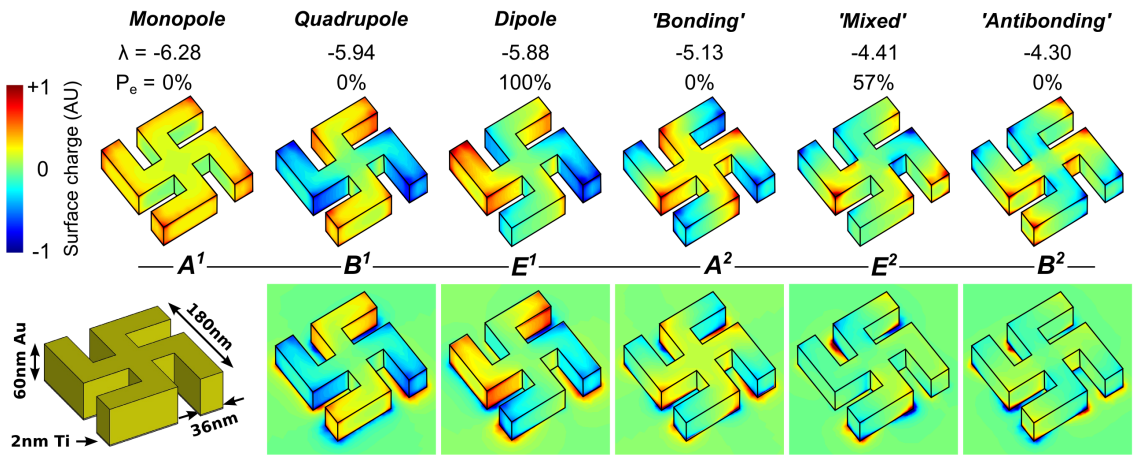

Figure 2: Lowest energy eigenmodes of (top row) an isolated ideal Au gammadion and (bottom row) the same gammadion supported by a Si_3N_4 membrane. The gammadion dimensions are illustrated in the bottom left panel. The mode symmetry, eigenvalue (λ) and the electric dipole moment (P_e) are also indicated.

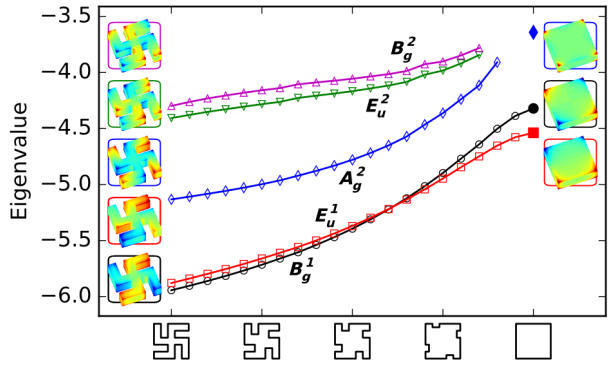

Figure 3: Alteration of mode energy and order in an 'ideal' gammadion through reduction in intra-structural coupling as the gammadion is morphed into a square. Inset are the schematics of the eigenmodes. Note that the 'bonding', 'mixed' and 'antibonding' modes are not supported by a simple square structure. However, a square edge-mode of equivalent symmetry (A^2) to the 'bonding' mode does exist (blue solid symbol). The solid symbols are those of the square, while the open symbols are those of the gammadia.

plane dipole results in fine splitting of the parent C_{4h} modes, creating 'proximal' and 'distal' modes, as previously observed in monochromated EELS in cuboidal structures.[36]

EELS Analysis

We now turn to an experimental analysis of a real gammadion, which will be used to improve the accuracy of simulations performed to assess mode properties such as the near-field strength and chirality that are otherwise inaccessible, and to understand the impact imperfections have on them.

In EELS measurements, the energy lost by the microscope's electron beam as it passes by or through a material is measured as the beam is scanned over the sample.[37] The resulting two-dimensional array of low-loss spectra can be collected with high spatial resolution, from which the plasmon resonances can be observed. Simultaneous to EELS acquisition, STEM images are acquired, allowing direct correlation between the real sample shape and the plasmonic modes. However, the resulting EELS maps should be interpreted with care because they don't directly reflect the charge distributions that one might intuitively expect to see. A loss map will show the excitation across the image, within a chosen energy slice. Each pixel indicates the strength of plasmonic coupling to the electron beam for a probe positioned at that point. Thus, if one were to consider a dipole excitation within a simple disc, the resulting map would be a broad *ring* of intensity, since positioning the electron beam at any point around the disc's circumference will excite a dipole mode, with charge distributed diametrically. In essence, EELS maps show the ensemble of all possible dipoles and, more generally, of all possible excitations, at that energy (we note, however, that shaping the electron beam using phase plates has recently been shown to overcome this limitation[38]). Similarly, in the case of the gammadion, the EELS map of the B^1 quadrupole mode will resemble that of the E^1 dipole mode because both involve charge distribution to the tips of the gammadion arms with a node in the centre of the structure. A second consideration is

that the nature of the EELS excitation differs from that by incident light radiation. EELS measurements are sensitive to the magnitude of the electric field component along the path of the beam and so do not directly measure the in-plane electric fields of bonding modes between neighbouring structures.[16,39]

Figure 4(a) shows five experimental EELS spectra collected from a number of electron beam positions, indicated in the inset, around a real gammadion fabricated using electron beam lithography with a thin Ti adhesion layer beneath the gold (see the Methods section for details). Accurate structural information from the STEM and EELS data was used to construct a 'real' structure, shown in Fig. 5(a), used in the boundary element calculations described below - more details are presented elsewhere.[19] The real gammadion has a number of the imperfections commonly seen in nanofabricated structures, including: a non-uniform thickness and edge profile from the granularity of the material; an enlarged central region and thinner arm tips due to over- and underexposure in the patterning process; rounding of corners; a sloped out-of-plane edge profile; edge roughness; and asymmetry in the arm shapes. Such imperfections can give rise to chiroptical phenomena,[40] shift mode energies and cause splitting of the modes, so it is crucial to characterise their influence.

The first four peaks in Fig. 4(a) correspond to excitation of distinct LSPR modes. The acquisition positions were selected by surveying the dataset to find maxima in energy loss profiles, which correspond to regions of charge accumulation and depletion during excitation. It is clear that the closely spaced modes 1 and 2 have the strongest interaction with the electron beam and lie within the infrared region. Although the peaks were collected from symmetrically-equivalent positions, they have subtly different spatial distributions that can be interpreted through the simulations described below. In fact, these simulations allow us to assign the first four peaks to the quadrupole, dipole, 'bonding' and 'mixed' plasmon modes, respectively, as indicated in the labels of Fig. 4(b). Fig. 4(b) presents loss maps showing the different spatial distributions and energies at the five experimentally observed loss peaks (Animated loss maps at all energies are included in Supporting Information.) These maps

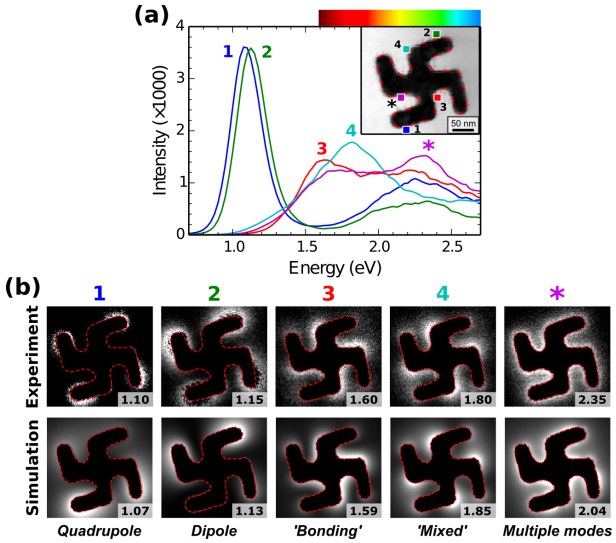

Figure 4: (a) Measured EELS spectra (after deconvolution and averaged over 3×3 pixels) at the probe positions indicated in the inset bright-field image. The corresponding photon color spectral range is indicated above. (b) Aloof EELS loss maps at the peak energies of the five lowest modes identified above in the (top row) experiment and (bottom row) simulation. In each panel, the nanostructure is masked within the dashed red lines and the contrast is maximised. The inset number is the mode energy in eV. Panels 1 and 2 are the integrated intensities derived from Lorentzian fits to the spectra shown in (a). All other panels show an energy window of 0.025 eV. The simulated loss maps are artificially broadened to match the experimental resolution (see Methods for details).

exclude data from the metal area in order to focus on 'aloof' excitation of plasmonic modes[37] and to avoid reduction in the signal-to-noise ratio due to high scattering rates within the gold film. There are clear maxima of the loss of the arms in the lowest modes and at the elbows in the higher energy modes, consistent with the states shown in the left and right columns of Fig. 1, respectively. The fifth peak, labelled with an asterisk, appears bright around the entire perimeter and is caused by an ensemble of distinct modes not resolved in the experiment.

Simulated loss maps (using the experimentally-measured 'real' shape) are shown in the second row of Fig. 4(b). These maps were calculated by constructing a simulation using information from the STEM data. The resulting maps are in excellent agreement with the experimental plasmon distribution data, accurately reproducing the asymmetries in the spatial distribution of the different modes, and the LSPR energies are consistent with experiment to within 0.05 eV. Such excellent agreement between simulation and experiment is only obtained when the exact structure is simulated.

Comparison of the 'real' and 'ideal' simulations allow a better understanding of which aspects of the imperfect structures have the greatest influence on their plasmonic response. Additionally, through simulation we can access finer details of the LSPRs than experimental resolution allows, and can assess the influence structural variations have on the energy, character, electric dipole moment, and the near-field strength and chirality of each mode. We simulated the responses of three structures, which are shown in Figure 5(a). In addition to the 'ideal' structure and the 'real' one derived from experiment, we included an intermediate 'rounded' structure, formed from four identical arms of uniform height but with rounded corners in the plane of the structure. The arms were formed by averaging the four individual arm outlines of the real structure, to give a slightly canted shape that retains overall four-fold rotational symmetry. Thus, comparison of 'ideal' and 'rounded' structures allows the impact of in-plane rounding to be assessed, whilst a comparison of 'rounded' and 'real' structures enables the effect of out-of-plane variations and a loss of rotational symmetry to be

examined. The average surface loss contribution to the EELS spectrum for each of the three structures (without experimental broadening to aid comparisons) is plotted in Figure 5(b). In agreement with the analysis presented above, we identify five spectral components in the three spectra, numbered as before. However, now we can resolve the loss peak from the fifth LSPR, the 'antibonding' mode, which exists on the onset of a broad peak that extends from 2.0 eV to above 2.5 eV, formed from multiple high order modes closely spaced in energy that will not be discussed further (see animations, simulated loss maps and tabulated resonance energies in Supporting Information).

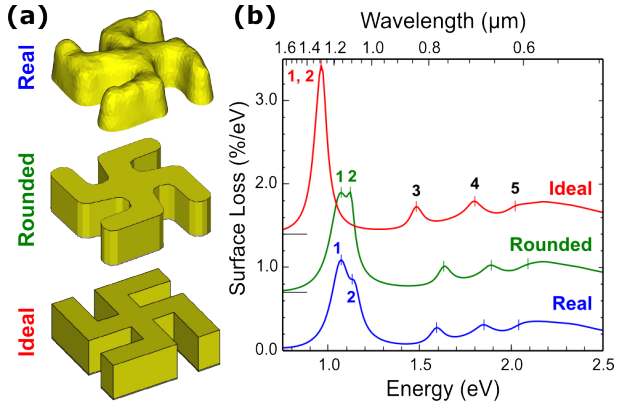

Figure 5: (a) 'Real', 'rounded' and 'ideal' structures used for analysis of the effects of imperfections on plasmonic response, drawn without substrate. (b) The simulated average EELS spectra for each of the three structures, showing the peak resonances, numbered 1 to 5. (Note that averaging over all electron beam positions eliminates finer details in the spatially resolved data, including mode splitting.)

There are two significant differences between the three spectra. First, the resonances of both the 'rounded' and 'real' structures are shifted to higher energies than those of the 'ideal' structure due to a decrease in the charge separation caused by the removal of sharp corners.[41] A second effect is a loss of the near-degeneracy of the closely spaced quadrupole- and dipole-like low-energy modes. It is interesting to note that this splitting does not require a reduction in the structure's symmetry, since both 'rounded' and 'ideal' structures share the same C_4 symmetry, yet the former has a clear separation of the modes labelled 1 and 2. Further modification of the arm shape to produce the 'real' structure then increases the splitting further.

The peak energies in the spectra from the 'real' structure match those from the 'rounded' one remarkably well, considering the very different out-of-plane profiles of the structure. This is because the modes are planar and hence the in-plane profile is more important than that out-of-plane when considering the character of the modes. That being said, it is of course true that out-of-plane asymmetries are crucial in giving rise to chiroptical phenomena.[40] Excluding the first two modes, the loss maps from the resonances of 'real' and 'rounded' structures (shown in Supporting Information Figure S4) are broadly similar, whilst the corresponding maps of the 'ideal' structure are more intense, due to the stronger field produced by the greater charge segregation into the sharp corners. For the 'real' structure, the loss maps become asymmetric, with more localised 'hot-spots', and there is a further reduction in loss intensity in all modes.

In addition to the separation of modes 1 and 2, the dipole-like mode (mode 2) and 'mixed' mode (mode 4) are both split further in the 'real' structure. In essence, the degenerate 'parent' E modes of the 'ideal' structure are split by asymmetric structural imperfections. Thus, the broadened peak labelled as 1 and 2 in the 'real' structure spectrum in fact contains three overlapping modes that are closely spaced in energy: a mode of quadrupole character and two modes resembling the parent dipole modes. The anisotropy of the modes is not clear from the average spectra but the modes could be stimulated independently by polarised light. The reduction in symmetry will also affect the strength and spatial distribution of the associated near-field, which is explored in maps of the near-field magnitudes above the sample in Supporting Information Figure S6.

To unambiguously distinguish the mode symmetries, the eigenmodes were determined for both the 'real' and 'rounded' structures and are shown in Figure 6. These maps can be compared with those in Fig. 2 and were used to assign the mode symmetries in Fig.4. Instead of strong, high-symmetry resonances across the entire structure, the imperfect gammadion has more localised charge distributions and apparent 'hot-spots' at the arm tips and elbows. The dipole moments, P_e, are also indicated alongside each mode. The dipole moments of

the 'rounded' structure are lower than those of the 'ideal' one, but the retention of C_{4h} symmetry means that optically dark modes are also retained. The main effect of structural imperfections in the 'real' structure, however, is to confer a degree of dipolar character on all of the low energy modes, which is important because it implies that all of these modes could be excited optically. For example, the moment of the quadrupole-like mode of the 'real' structure is increased from zero in the 'ideal' structure to about half of that of the 'ideal' E^1 modes. In fact, the average dipole moment over all displayed modes is 63 % higher in the 'real' structure than in the 'ideal' structure. Such large changes in mode properties with subwavelength-scale structural deviations are in stark contrast to those in somewhat similar but simpler split ring resonator structures,[3] and is due to the far larger role that *intra*-structural coupling plays in the nature of the gammadion modes.

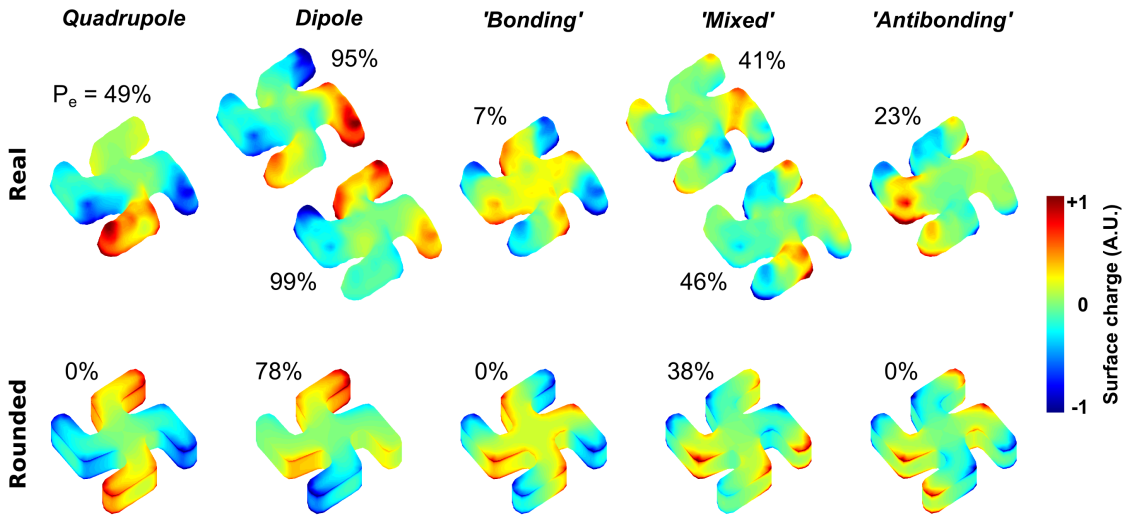

Figure 6: Lowest energy eigenmodes of the (top row) 'real' and (bottom row) 'rounded' gammadia showing the individually normalised surface charge densities ordered by eigenvalue and grouped by symmetry (*c.f.* the 'ideal' eigenmodes of Fig. 2). The electric dipole moment, P_e, of each mode is shown relative to the E^1 mode of the 'ideal' structure. Note that only one each of the identical and degenerate 'bonding' and 'antibonding' modes are shown for the 'rounded' structure.

In general, there is a clear relation between the 'real' structure modes and those of the 'parent' ideal gammadion of Fig. 2. For example, the quadrupole-like mode remains of lower energy than the doubly-degenerate dipole-like modes, and the latter retain almost full dipolar

polarization. Also apparent at higher energies are modes that retain the appearance of the 'bonding', 'mixed' and 'antibonding' modes. The 'bonding' mode is more robust to the effects of imperfections and still does not have a strong dipolar character; the 'mixed' modes only drop slightly in dipole moment, while the 'antibonding' modes significantly increase with respect to those 'ideal' modes in Fig. 2. All of these changes in spatial distribution and polarization between the modes of Fig. 2 and Fig. 6 are caused by structural imperfections and will alter the near-field distribution which governs the structure's interaction with light and matter and so ultimately governs the material's functionality. Indeed, as shown in Supporting Information Figure S8, the mode energy shifts and peak splitting seen in the EELS data are reproduced in the optical scattering cross-sections from the 'real' and 'ideal' gammadia and, in the 'real' structure, the coupling to light is anisotropic due to different split modes and nominally dark modes being excited at different light polarisation angles with respect to the structure.

Finally, we consider the chiral nature of the field produced by the gammadion, which underlies its potential use in a wide number of applications. The electromagnetic field distribution in any given structure will be influenced by the nature and direction of the stimulation, but it will ultimately be dependent on the modes of the structure. As a measure of the chirality of the field from different modes, we plot in Figure 7 the electric field contribution to the chirality by using the parameter $E \cdot \nabla \times E$, where E is the electric field in a plane 15 nm above the sample. We note that while this omits the magnetic contribution to a full calculation of chirality,[14] these structures are small enough to fall within the quasistatic limit where electrostatic calculations yield good approximations and that this approach allows examination of the properties of individual modes. Inclusion of an additional $B \cdot \nabla \times B$ term to calculate the spatial density of the conserved quantity used by Lipkin[42] is not expected to alter qualitatively the symmetry of the results. It is clear from the figure that the chirality of the field has similar distributions for similar modes across the different structures, but is greatly reduced in the 'real' and 'rounded' structures and is asymmetric in the 'real'

structure, as one would expect. Interestingly, the near field chirality of the higher order modes ('bonding' through to 'antibonding') in the 'ideal' and 'rounded' structures appears stronger than that of the lower order modes, most likely as a result of the lower surface charge antinode spacing. While this observation is of importance in the design of structures intended to be used for the chiral fields they support, this increase in chirality does not seem to be carried over to the 'real' structure due to symmetry reduction; hot spots resulting from the structural asymmetry dominate the chirality maps.

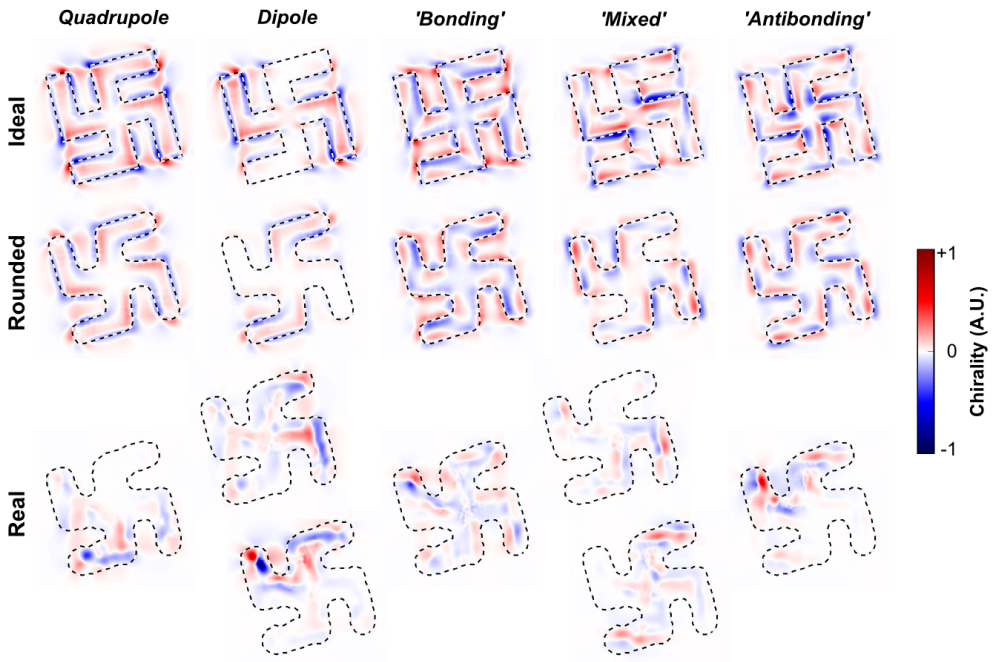

Figure 7: Chirality of the electric field in a plane 15 nm above sample in the eigenmode simulations of 'real', 'rounded' and 'ideal' structures. A common normalization is used across all data.

We also note that the symmetry of the gammadion and the nature of the modes it supports gives rise to an interesting property whereby the electric field distribution in the tip-elbow 'antibonding' mode is the approximate reverse of that in the quadrupole-like mode, as shown in the top row of Figure 8. The chirality of the field in this symmetric structure, shown in the bottom row, is similarly approximately inverted, and although both modes are dark in the 'ideal' structure, the imperfections of the 'real' structure imbue a weak dipole moment that could be coupled to optically. Alternatively, the dark (or gray) gammadion

modes may be excited through near-field coupling from an adjacent structure.[43] The results therefore indicate that the chirality of the fields produced by plasmonic modes of gammadia can be wavelength-dependent. Indeed, to the authors' knowledge, no single structure other than the gammadion supports such a complete swapping of field chirality direction upon simply changing the mode being excited.

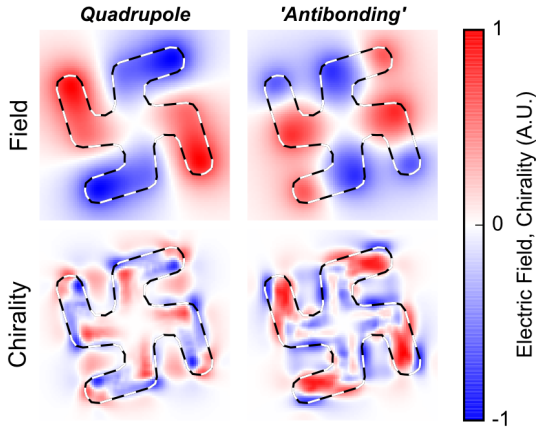

Figure 8: Z-component of the electric field (top row) and its chirality (bottom row) of the quadrupole-like and 'antibonding' modes of the 'rounded' structure, showing the approximate reversal of the field pattern and chirality. A small out out-of-plane rounding has been added to remove hot spots arising from sharp edges. In all images the data are calculated in a plane 15 nm above the sample surface.

Conclusions

All metamaterial elements are sensitive to variations in structure but concave chiral elements supporting intra-structural coupling are particularly sensitive. Since the chirality of the field and its interaction with matter underlies many potential applications of chiral metamaterials, it is particularly important to understand the impact of imperfections. Here, we have characterised the plasmonic modes of a symmetric planar gammadion structure and found the lowest order modes are a near-degenerate quadrupole-like mode and a dipole-like one, with the higher order modes characterised by the arm tip-elbow coupling order. The near-degenerate modes are split by the inclusion of small, subwavelength-scale deviations from

the ideal structure that retains the symmetry but alters intrastructural coupling. Similarly small deviations in the structure resulting from fabrication limitations give rise to symmetry reduction that alters the spatial shape of the modes and the resulting near-field distributions, magnitudes and chirality strengths, shifts their energies, and can transform dark modes into bright ones. By using the experimental data to inform realistic simulations, STEM-EELS provides a very powerful method to assess the impact of structural variation in plasmonic metamaterial elements.

Supporting Information Available

The following supporting information is available: examples of concave and convex structures (Fig. S1); further discussion of the modes of assemblies of concave structures (Fig. S2), including simulations where intra-structural coupling in the gammadion is modified (Fig. S3); static (Fig. S4) and animated experimental and simulated loss maps; tabulated resonance energies; further evidence of mode splitting (Figs. S5-S6); and simulated near-field maps (Fig. S7) and optical scattering cross-sections (Fig. S8) of the different structures.

This material is available free of charge via the Internet at `http://pubs.acs.org/`.

Acknowledgement

This work was supported by the Engineering and Physical Sciences Research Council (EPSRC) of the UK under grants EP/L001969/1 and EP/M024423/1. Original data files are available at [doi:TBA].

References

(1) Yao, K.; Liu, Y. Plasmonic Metamaterials. *Nanotechnol. Rev.* **2014**, *3*, 177–210.

(2) Garcia, M. A. Surface Plasmons in Metallic Nanoparticles: Fundamentals and Applications. *J. Phys. D Appl. Phys.* **2011**, *44*, 283001.

(3) Boudarham, G.; Feth, N.; Myroshnychenko, V.; Linden, S.; de Abajo, J. G.; Wegener, M.; Kociak, M. Spectral Imaging of Individual Split-ring Resonators. *Phys. Rev. Lett.* **2010**, *105*, 255501.

(4) Schmidt, F. P.; Ditlbacher, H.; Hofer, F.; Krenn, J. R.; Hohenester, U. Morphing a Plasmonic Nanodisk into a Nanotriangle. *Nano Lett.* **2014**, *14*, 4810–4815.

(5) Huang, W.-X.; Zhang, Y.; Tang, X.-M.; Cai, L.-S.; Zhao, J.-W.; Zhou, L.; Wang, Q.-J.; Huang, C.-P.; Zhu, Y.-Y. Optical Properties of a Planar Metamaterial with Chiral Symmetry Breaking. *Opt. Lett.* **2011**, *36*, 3359–3361.

(6) Liu, Y. J.; Wu, S.; Popp, D.; Leong, E. S. P.; Hor, Y. L.; Phua, W. K.; Mok, K. L.; Teng, J. H.; Robinson, R.; Li, E. P. et al. Effect of Asymmetrical Nanostructures on Detecting the Optical Rotational Properties of Large Biofilament Structures. Plasmonics: Metallic Nanostructures and Their Optical Properties XI. 2013.

(7) Canfield, B. K.; Kujala, S.; Laiho, K.; Jefimovs, K.; Turunen, J.; Kauranen, M. Chirality Arising from Small Defects in Gold Nanoparticle Arrays. *Opt. Express* **2006**, *14*, 950–955.

(8) Schäferling, M.; Dregely, D.; Hentschel, M.; Giessen, H. Tailoring Enhanced Optical Chirality: Design Principles for Chiral Plasmonic Nanostructures. *Phys. Rev. X* **2012**, *2*, 031010.

(9) Bai, B.; Svirko, Y.; Turunen, J.; Vallius, T. Optical Activity in Planar Chiral Metamaterials: Theoretical Study. *Phys. Rev. A* **2007**, *76*, 023811.

(10) Krasavin, A. V.; Schwanecke, A. S.; Zheludev, N. I. Extraordinary Properties of Light Transmission Through a Small Chiral Hole in a Metallic Screen. *J. Opt. A: Pure Appl. Opt.* **2006**, *8*, S98.

(11) Hendry, E.; Carpy, T.; Johnston, J.; Popland, M.; Mikhaylovskiy, V. R.; Lapthorn, J. A.; Kelly, M. S.; Barron, D. L.; Gadegaard, N.; Kadodwala, M. Ultrasensitive Detection and Characterization of Biomolecules Using Superchiral Fields. *Nat. Nano.* **2010**, *5*, 783–787.

(12) Tullius, R.; Karimullah, A. S.; Rodier, M.; Fitzpatrick, B.; Gadegaard, N.; Barron, L. D.; Rotello, V. M.; Cooke, G.; Lapthorn, A.; Kadodwala, M. "Superchiral" Spectroscopy: Detection of Protein Higher Order Hierarchical Structure with Chiral Plasmonic Nanostructures. *J. Am. Chem. Soc.* **2015**, *137*, 8380–8383.

(13) Jack, C.; Karimullah, A. S.; Leyman, R.; Tullius, R.; Rotello, V. M.; Cooke, G.; Gadegaard, N.; Barron, L. D.; Kadodwala, M. Biomacromolecular Stereostructure Mediates Mode Hybridization in Chiral Plasmonic Nanostructures. *Nano Lett.* **2016**, *16*, 5806–5814.

(14) Tang, Y.; Cohen, A. E. Optical Chirality and Its Interaction with Matter. *Phys. Rev. Lett.* **2010**, *104*, 163901.

(15) Hendry, E.; Mikhaylovskiy, R. V.; Barron, L. D.; Kadodwala, M.; Davis, T. J. Chiral Electromagnetic Fields Generated by Arrays of Nanoslits. *Nano Lett.* **2012**, *12*, 3640–3644.

(16) Chu, M.-W.; Myroshnychenko, V.; Chen, C. H.; Deng, J.-P.; Mou, C.-Y.; de Abajo, F. J. G. Probing Bright and Dark Surface-plasmon Modes in Individual and Coupled Noble Metal Nanoparticles Using an Electron Beam. *Nano Lett.* **2009**, *9*, 399–404.

(17) García de Abajo, F. J. Optical Excitations in Electron Microscopy. *Rev. Mod. Phys.* **2010**, *82*, 209–275.

(18) Kociak, M.; Stephan, O. Mapping Plasmons at the Nanometer Scale in an Electron Microscope. *Chem. Soc. Rev.* **2014**, *43*, 3865–3883.

(19) Paterson, G. W.; Karimullah, A.; Williamson, S.; Kadodwala, M.; MacLaren, D. A. Electron Energy Loss Spectroscopy of a Chiral Plasmonic Structure. *J. Phys. Conf. Ser.* **2015**, *644*, 012005.

(20) Boersch, H. Experimentelle Bestimmung der Energieverteilung in thermisch ausgelösten Elektronenstrahlen. *Z. Phys.* **1954**, *139*, 115–146.

(21) Knauer, W. Boersch Effect in Electron–optical Instruments. *J. Vac. Sci. Technol.* **1979**, *16*, 1676–1679.

(22) Gloter, A.; Douiri, A.; Tencé, M.; Colliex, C. Improving Energy Resolution of EELS Spectra: an Alternative to the Monochromator Solution. *Ultramicroscopy* **2003**, *96*, 385–400.

(23) Hohenester, U.; Trügler, A. MNPBEM – A Matlab Toolbox for the Simulation of Plasmonic Nanoparticles. *Comput. Phys. Commun.* **2012**, *183*, 370–381.

(24) Hohenester, U. Simulating Electron Energy Loss Spectroscopy with the MNPBEM Toolbox. *Comput. Phys. Commun.* **2014**, *185*, 1177–1187.

(25) García de Abajo, F. J.; Howie, A. Retarded Field Calculation of Electron Energy Loss in Inhomogeneous Dielectrics. *Phys. Rev. B* **2002**, *65*, 115418.

(26) Johnson, P. B.; Christy, R. W. Optical Constants of the Noble Metals. *Phys. Rev. B* **1972**, *6*, 4370–4379.

(27) Siegfried, T.; Ekinci, Y.; Martin, O. J.; Sigg, H. Engineering Metal Adhesion Layers That Do Not Deteriorate Plasmon Resonances. *ACS Nano* **2013**, *7*, 2751–2757.

(28) Möbius, J.; Kobbelt, L. In *Curves and Surfaces: 7th International Conference, Avignon, France, June 24 - 30, 2010, Revised Selected Papers*; Boissonnat, J.-D., Chenin, P., Cohen, A., Gout, C., Lyche, T., Mazure, M.-L., Schumaker, L., Eds.; Springer Berlin Heidelberg: Berlin, Heidelberg, 2012; pp 488–500.

(29) Hyperspy: Multi-dimensional Data Analysis Toolbox. http://hyperspy.org (accessed January 25, 2018).

(30) Awada, C.; Popescu, T.; Douillard, L.; Charra, F.; Perron, A.; Yockell-Lelièvre, H.; Baudrion, A.-L.; Adam, P.-M.; Bachelot, R. Selective Excitation of Plasmon Resonances of Single Au Triangles by Polarization-Dependent Light Excitation. *J. Phys. Chem. C* **2012**, *116*, 14591–14598.

(31) Gómez, D. E.; Vernon, K. C.; Davis, T. J. Symmetry Effects on the Optical Coupling Between Plasmonic Nanoparticles with Applications to Hierarchical Structures. *Phys. Rev. B* **2010**, *81*, 075414.

(32) Schmidt, F.-P.; Ditlbacher, H.; Hohenester, U.; Hohenau, A.; Hofer, F.; Krenn, J. R. Dark Plasmonic Breathing Modes in Silver Nanodisks. *Nano Lett.* **2012**, *12*, 5780–5783.

(33) Bellido, E. P.; Manjavacas, A.; Zhang, Y.; Cao, Y.; Nordlander, P.; Botton, G. A. Electron Energy-Loss Spectroscopy of Multipolar Edge and Cavity Modes in Silver Nanosquares. *ACS Photonics* **2016**, *3*, 428–433.

(34) Campos, A.; Arbouet, A.; Martin, J.; Gérard, D.; Proust, J.; Plain, J.; Kociak, M. Plasmonic Breathing and Edge Modes in Aluminum Nanotriangles. *ACS Photonics* **2017**, *4*, 1257–1263.

(35) Prodan, E.; Radloff, C.; Halas, N. J.; Nordlander, P. A Hybridization Model for the Plasmon Response of Complex Nanostructures. *Science* **2003**, *302*, 419–422.

(36) Nicoletti, O.; de la Peña, F.; Leary, R. K.; Holland, D. J.; Ducati, C.; Midgley, P. A. Three-dimensional Imaging of Localized Surface Plasmon Resonances of Metal Nanoparticles. *Nature* **2013**, *502*, 80–84.

(37) Egerton, R. F. *Electron Energy-loss Spectroscopy in the Electron Microscope*, 3rd ed.; Springer: New York, 2011.

(38) Guzzinati, G.; Béché, A.; Lourenço-Martins, H.; Martin, J.; Kociak, M.; Verbeeck, J. Probing the Symmetry of the Potential of Localized Surface Plasmon Resonances with Phase-shaped Electron Beams. *Nat. Commun.* **2017**, *8*, 14999.

(39) Hohenester, U.; Ditlbacher, H.; Krenn, J. R. Electron-energy-loss Spectra of Plasmonic Nnanoparticles. *Phys. Rev. Lett.* **2009**, *103*, 106801.

(40) Arteaga, O.; Sancho-Parramon, J.; Nichols, S.; Maoz, B. M.; Canillas, A.; Bosch, S.; Markovich, G.; Kahr, B. Relation Between 2D/3D Dhirality and the Appearance of Chiroptical Effects in Real Nanostructures. *Opt. Express* **2016**, *24*, 2242–2252.

(41) Wiley, B. J.; Im, S. H.; Li, Z.-Y.; McLellan, J.; Siekkinen, A.; Xia, Y. Maneuvering the Surface Plasmon Resonance of Silver Nanostructures Through Shape-controlled Synthesis. *J. Phys. Chem. B* **2006**, *110*, 15666–15675.

(42) Lipkin, D. M. Existence of a New Conservation Law in Electromagnetic Theory. *J. Math. Phys.* **1964**, *5*, 696–700.

(43) Hentschel, M.; Weiss, T.; Bagheri, S.; Giessen, H. Babinet to the Half: Coupling of Solid and Inverse Plasmonic Structures. *Nano Lett.* **2013**, *13*, 4428–4433.

TOC Graphic

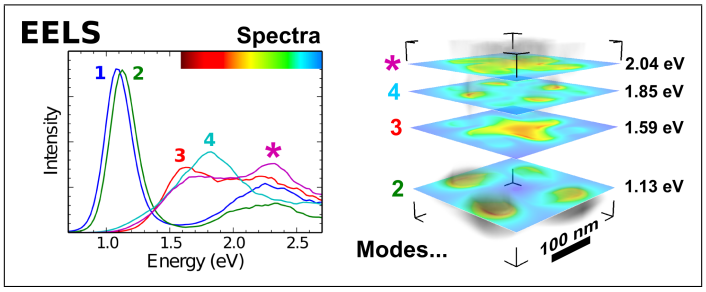
EELS
Spectra
Intensity
1
2
3
4
*
1.0
1.5
2.0
2.5
Energy (eV)
2.04 eV
1.85 eV
1.59 eV
1.13 eV
Modes...
100 nm